

Chapter 2

New Advances in the Production of Iron-Based Nanostructures Manufactured by Laser Pyrolysis

Ion Morjan and Rodica Alexandrescu

Abstract Nanoparticles (NPs) are submicron moieties made of inorganic or organic materials, which have many novel properties compared with their bulk counterparts. The CO₂ laser pyrolysis of gas- and vapor-phase reactants offers an approach for the synthesis of uniform nanoparticles. The synthesis of iron oxide-based nanomaterials by laser pyrolysis has been achieved by a handling procedure, in which the oxidation process initiates and develops inside the laser-induced reaction zone. In a second step, a more complex experimental procedure is used, in which the iron precursor is allowed to dissociate alone in the flame with a surrounding oxidizing atmosphere. XRD and TEM analyses reveal a major content of maghemite/magnetite in samples SF. The power density and the nozzle diameter influence the particle size.

2.1 Introduction

Nanoparticles (NPs) are submicron moieties made of inorganic or organic materials, which have many novel properties compared with their bulk counterparts (Einar Kruis et al. 1998). Their diameters usually range from 1 to 100 nm, although there are examples of NPs several hundreds of nanometers in size. Magnetic NPs have many unique magnetic properties such as superparamagnetism, low Curie temperature, and high magnetic susceptibility. Magnetic NPs are of great interest for researchers from a broad range of disciplines, including magnetic fluids, data storage, catalysis, and bioapplications (Cristina Blanco-Andujar et al. 2010). Currently, magnetic NPs are used in important bioapplications, including magnetic bioseparation and detection of biological entities (cells, proteins, nucleic acids, enzymes, bacteria, viruses, etc.), clinic diagnosis and therapy (such as

I. Morjan (✉) · R. Alexandrescu
National Institute for Laser, Plasma & Radiation Physics, Atomistilor St. 409,
Bucharest, Romania
e-mail: Ion.morjan@infpr.ro

Magnetic Resonance Imaging) (Nydeia et al. 2013) and in order to reduce the toxicity associated with cytotoxic drugs (Baena and Marulanda 2011).

Iron-based nanomaterials (Abhilash et al. 2011) have found applications in many areas of science and technology due to their unique magnetic properties. A size reduction of these materials from bulk to the nanoscale allows them to display various size related properties. Among other changes, a significant decrease in size can alter reactivity, increase surface area and change the magnetic properties. The use of magnetic nanoparticles as molecular imaging probes enables noninvasive in vivo studies of antigen expression of diseases in various internal organs. Particularly, iron oxide nanoparticles (Shikwambana et al. 2011) with new subsequent functionalized procedures permit applications, such as conjugation of DNA, antibodies, proteins, etc. However, the synthesis of high-quality functionalized magnetic iron oxide NPs with tunable sizes and shapes in a controlled manner is still a challenge. The magnetic properties and function of naked or surface functionalized iron oxide NPs depend on their physical properties: their size, shape, microstructure, and the chemical phase in which they are present. A number of chemical methods are available and are extensively used for the synthesis of iron-based nanostructures, but these are often energy intensive and employ toxic chemicals. Despite the availability of chemical methods, the production of large amounts of pure, nonagglomerated NPs, with desired size and narrow size distribution, still proves to be an extremely difficult task.

The CO₂ laser pyrolysis of gas- and vapor-phase reactants offers an alternative approach for the synthesis of uniform nanoparticles (Cannon et al. 1982; Swihart 2003). This technique is mainly developed for its advantages of residing; (i) the well-defined interaction volume where no interaction with the reactor chamber walls and hence, no contamination occurs and (ii) the production of very fine particles (usually less than 50 nm). The laser pyrolysis belongs to the synthesis methods that function via a homogeneous nucleation in the gas phase (Srdic et al. 2000).

The current technology of laser pyrolysis is depicted below as is the preparation of iron-based nanostructures. In this paper, examples of laser pyrolysis processes of Fe(CO)₅-based gas mixtures will be presented. In parts these examples rely on our previous reported results. Therefore, the phenomenology of the process and the characterization of nanopowder structures is described. Some characteristics of the laser-sensitized pyrolysis for producing iron oxides in the gamma phase will be discussed. Using Fe(CO)₅ mixed with hydrocarbon precursors and a particular irradiation geometry, iron particles embedded in carbon sheets were obtained.

2.2 The Laser Pyrolysis

2.2.1 Process Description

Laser pyrolysis is based on the overlapping of the emission line of the laser with an absorption line of one or more precursors. The 10P(20) CO₂ laser line peaks at 10.591 μm and is the strongest emission line. An additional substance, the

so-called sensitizer is used in the case of nonabsorbing gas precursors. It absorbs the energy and transmits it to the precursors by collisions. As a final effect of a laser-absorbing system coupling, the laser acts as a heat source. When exposed to the laser and the prevalent gas pressure, the time between absorption of photons by the reactant gases is much greater than that necessary for distribution of the energy to nearby gas molecules through collisions. Thus, a thermal equilibrium is achieved. In this case, only one of the gas species needs to absorb the laser energy, since the others will be heated by collisions. The system is based on a cross-flow configuration. The reactant flow emerges in the reactor through a nozzle system where it is orthogonally intersected by the focused IR radiation beam. Pyrolysis in the gas phase occurs in the small volume defined by the crossing of the radiation gases, where usually a “flame” appears.

From the point of view of IR photochemistry, basic principles of the laser pyrolysis rely on (i) the resonant absorption of photons by IR-active vibrational modes of molecules in ground electronic state; (ii) collision-aided vibrational energy transfer towards the translational and rotational degrees of freedom and (iii) the heating of the reactant gases and dissociation, followed by nucleation and growth of aggregates.

Nanoparticle formation starts after reaching the degree of supersaturation of condensable products in the vapor phase. The condensable products result from the laser-induced chemical reactions that occur at the intersection point of the laser beam with the molecular flow of gas or vapor-phase precursors. Particle nucleation and growth are complex processes, which usually depend on reaction pathways given by the specific experimental conditions (particularly, the nature and number of reactants). Particles grow by collisions (the growth is proportional to the system pressure) and by coalescence. Nondispersible aggregates are formed. Once time intervals between collisions are too short to form dense spherical particles, agglomerates form. The confinement of the gas precursors and of the newly nucleated particles toward the flow axis is achieved by a coaxial argon flow. Nucleated particles are kept together by the gas stream and collected in a removable tank at the exit of the reaction cell. Alternatively, the particles may be deposited on a substrate positioned in the flow reactor. The main process parameters are: the nature of the gas (vapor) precursors, the gas flow rate, the pressure as well as the laser wavelength and power. For liquid precursors, the bubbled vapors are carried into the reaction zone by a carrier gas.

2.2.2 Advantages and Drawbacks

One clear advantage of laser pyrolysis over competing techniques is the high versatility that allows the production of a wide range of nanopowders iron and carbon-based, oxide semiconductors, metal-based, polymer nanocomposites, etc. Laser pyrolysis from the gas phase is a vapor-phase method of synthesis where the reactants are dilute and therefore yield a fine, loosely agglomerated powder,

narrow particle size distributions and controlled purity. Unlike furnace-heated, RF-heated and arc-plasma-heated processes, laser pyrolysis develops almost ideal thermal profiles and a reaction zone, which permits uniform nucleation and growth. As another advantage, this method generates ultrafine powders in a continuous way with narrow particle size distribution. The absence of potentially toxic surfactants makes the product ideal for the preparation of colloidal dispersions for use in biomedical applications (Bomatí-Miguel et al. 2010). It is of particular interest in the case of the iron nanoparticles due to their high magnetic response. The drawbacks of the laser pyrolysis technique are the constraints imposed on the reactants: the required elements must be present in a vapor phase and at least one reactant must contain an infrared absorption band for coupling the energy with the laser beam.

2.2.3 Characterization Techniques of the as-Synthesized Iron-Based Nanostructures

After synthesis, the morphology and composition of the iron oxide nanopowders were characterized by transmission electron microscopy (TEM), selected area electron diffraction (SAED), X-ray diffraction (XRD), energy dispersive X-ray analysis (EDX), and Mössbauer spectroscopy. The crystalline phases of the specimens (samples) were determined by XRD. The samples were scanned from $2\theta = 20$ to 85° on a computer-controlled DRON DART UM2 diffractometer with a graphite monochromatized $\text{CuK}\alpha$ radiation in a step scan mode, with a step width of 0.050 and an acquisition time on each step of 5 s. For the phase identifications, the JCPDS file system was applied. The crystallite sizes were evaluated applying the Scherrer formula to the full width at half maximum (FWHM) of selected peaks. The instrumental errors are corrected beforehand. The FWHM values were extracted from the fitted profile spectra using Voigt functions. EDX was performed with an accuracy of 0.5 %, with a SiLi detector from EDAX Inc. inside a scanning electron microscope model Inspect S from FEI. The powdery deposits were imaged in a transmission electron microscope Philips CM120ST (Customized Microscope 120 Super Twin, 120 kV max. acceleration voltage, about 2 Å resolution, $\text{Cs} = \sim 1.2$ mm). The samples were analyzed by the different electron microscopy techniques such as Bright Field TEM, SAED and HRTEM. The magnetization curves of nanopowders were determined using a vibrating sample magnetometer [VSM 880 ADE-DMS (USA)]. ^{57}Fe Mössbauer spectroscopy was used for analyzing the samples at temperatures ranging from 80 to 280 K. Mössbauer spectra were collected in transmission geometry by inserting the sample in a liquid nitrogen bath cryostat. A Mössbauer drive system operating in constant acceleration mode combined with conventional electronics and a ^{57}Co (Rh matrix) source of about 25 mCi activity, were used.

2.3 Nanostructured Iron Oxides

2.3.1 *State of the Art*

Very fine iron oxide nanoparticles have been the subject of numerous investigations and synthesis methods and drawn high interest with regards to the material science and their applications. Concerning the synthesis of ultrafine iron-oxide particles, several development routes have been followed so far. Methods such as conventional chemical processes, microwave plasma, pulsed laser ablation, pulsed laser-induced reaction, aerosol pyrolysis and continuous laser pyrolysis have been used.

In the following, the preparation and characterization of nano iron oxide-based materials obtained by three different handling procedures, is described: (a) The standard experimental procedure in which the oxidation process initiates and develops inside the laser-induced reaction zone by the simultaneous adduction of iron precursors and oxidizing agent (air); (b) A more complex experimental procedure in which the iron precursor is allowed to dissociate alone in the flame with a surrounding oxidizing atmosphere; (c) Core-shell iron-iron oxide nanoparticles using a variable nozzle geometry in which the established flows of precursor gases could maximize the desired particle morphology.

2.3.2 *Iron Oxide Nanoparticles Obtained by Laser Pyrolysis Procedures*

2.3.2.1 Iron Oxide Nanoparticles Obtained by Standard Laser Pyrolysis Procedure (SF-Type Samples)

In Fig. 2.1, a schematic general-purpose laser pyrolysis installation is depicted.

The flow reactor is the core of the laser pyrolysis technique, ensuring the practical application of the characteristic interplay between resonant and non-resonant processes. It was presented in details elsewhere (Majima et al. 1993). By using the same reactor set-up, the gas handling procedure of the active gas supply was varied, in order to modify the oxidation conditions. In a first set of experiments (labeled SF), a standard procedure was applied, in which the oxidation process initiates and develops inside the laser-induced reaction zone (the volume delimited by the crossing of the radiation beam and the flow of reactive gases emerging through the nozzles where usually “a flame” appears). For producing iron oxide nanopowders in the standard procedure, the focused continuous wave CO₂ laser radiation (70 W maximum output power, $\lambda = 10.6 \mu\text{m}$) orthogonally was made to cross the gas flows emerging through two concentric nozzles. The gas mixture which contained air and Fe(CO)₅ vapors (about 25 Torr vapor pressure at 20 °C) entrained by C₂H₄ was admitted through the central inner tube.

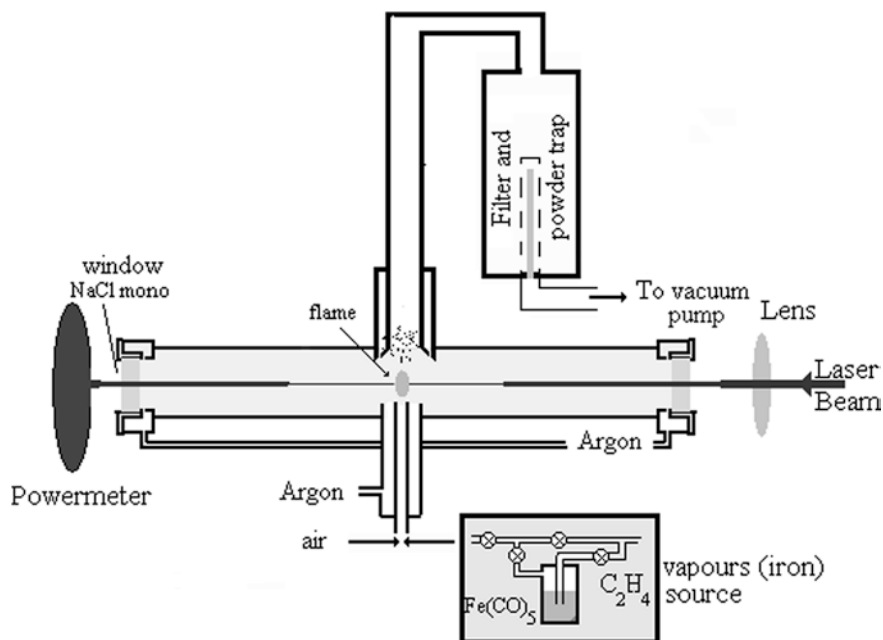


Fig. 2.1 Experimental set-up for obtaining nanometric iron oxides in a standard procedure

Table 2.1 Experimental parameters for the synthesis of iron oxides (SF- and F-type samples)

Sample	ϕ_{air} (sccm)	$\phi_{\text{C}_2\text{H}_4}$ (sccm)	P_L (W)	p kPa (mbar)
SF32	72	145	35	30 (300)
SF30	72	145	55	30 (300)
F5	100	300	25	30 (300)
F3	100	300	65	30 (300)

The confinement of gas precursors and of the freshly nucleated particles toward the flow axis is achieved by a coaxial argon flow. Iron oxide samples (SF32 and SF30) were obtained by varying the laser power between 35 and 55 W as presented in Table 2.1. The other experimental conditions, namely the reactor pressure, the relative flow of the oxidizing agent (air) and the flow of ethylene (as $\text{Fe}(\text{CO})_5$ carrier), were maintained constant at 300 mbar, 70 and 145 sccm, respectively. In order to prevent the NaCl windows from being coated with powder they were continuously flushed with Argon.

2.3.2.2 Iron Oxide Nanoparticles Obtained by Laser Pyrolysis in a “Soft” Oxidation Procedure (F-Type Samples)

In a second set of experiments (labeled F), the vapors of $\text{Fe}(\text{CO})_5$ (the iron precursor) entrained by ethylene emerge alone through the nozzle into the reaction chamber and are allowed to dissociate in the flame. At the same time, air (the

oxidizer agent) is introduced through the lateral outlets (100 sccm, located near the entrance windows), filling the entire reaction chamber, surrounding the flame and ensuring the oxidizing atmosphere for the freshly born iron fragments. A somehow similar procedure was applied by Veintemillas et al. (2001) and was termed “soft” oxidation. However, many experimental features (arrangement of gas flows and experimental parameters) in the actual procedure are different from (Kuncser et al. 2007). Thus, the iron fragments could suffer major oxidation after the laser focal point. The two representative F samples discussed here were obtained at different laser power densities (25 and 65 W). The pressure and carbonyl flow were kept constant. The experimental parameters needed for the preparation of both types of samples are presented in Table 2.1. Additional thermal treatment was applied to sample F5, by heating it in synthetic dry air. For this purpose, the temperature was increased at a rate of 20 °C/h, either to 120 °C or to 185 °C and maintained at these maximum temperatures for 2 h. The heated sample at 185 °C is hereafter labeled F5-185.

2.3.3 XRD Analysis of Nanoparticles

2.3.3.1 XRD Analysis of SF Nanoparticles

XRD analyses of SF nanoparticles are presented in Fig. 2.2. They exhibit rather broad peaks which could be assigned to the spinel-like iron (III) oxide, namely maghemite/magnetite iron phase. It is known that XRD alone is unable to differentiate between maghemite $\gamma\text{-Fe}_2\text{O}_3$ and magnetite Fe_3O_4 phases. The values of the

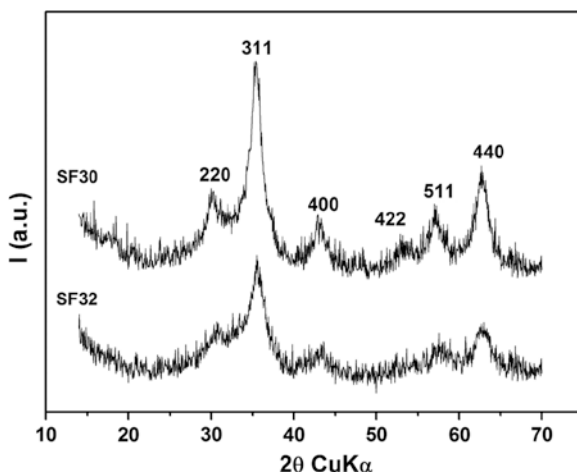


Fig. 2.2 Superposed X-ray diffractograms for SF iron oxide nanoparticles obtained at different laser powers (55 W-upper curve and 35 W-lower curve)

Table 2.2 Mean particle dimensions of the SF and F iron oxide nanoparticles, as estimated from XRD and TEM analysis

Sample	Scherrer crystallite dimensions D (nm) (from XRD analysis)			Mean particle diameter d_m (nm) (maxima of log normal distributions from TEM analysis)
	γ -Fe ₂ O ₃ /Fe ₃ O ₄	α -Fe	Fe ₃ C	
SF32	3			4.5
SF30	4.2			5.9
F5	3.8	9.4	–	9.3
F3	4.4	14.4	13.0	10.6
F5 -185 °C	17.8	–	–	14.6

unit cell parameter **a**, as estimated from the (220) (311) (511) (440) reflections are $a = 0.836$ nm and $a = 0.837$ nm for samples SF30 and SF32, respectively.

The Scherrer crystallite dimensions for samples SF30 and SF32 are approximately 4.2 and 3 nm (Table 2.2).

The broadness of the diffraction lines may be associated with the formation of very small particles as well as with a high degree of structural/crystallographic disorder. The XRD analysis differentiates between the primary crystallites, which could further form agglomerates, but does not reveal extremely small particles, the so-called “amorphous” to XRD ones. For the samples prepared above the Scherrer crystallite dimensions measured via XRD are consistent with the mean particle dimensions measured via TEM analysis (Table 2.2), which suggests that the samples are formed mainly from primary particles.

2.3.3.2 XRD Analysis of F-Type Nanoparticle

XRD analysis of F-type nanoparticles is summarized in Fig. 2.3. The samples consist of a mixture of three iron-based phases: γ -Fe₂O₃/Fe₃O₄ iron oxide, cementite Fe₃C and rather low-intensity, metallic Fe phase. The cementite Fe₃C phase is present in the sample as a mixture of both Fe₃C 34-0001 and Fe₃C 35-0772 (according to JCPDS file system). The corresponding peaks are marked in Fig. 2.3. The evaluation of the Scherrer mean crystallite size of sample F3 (Table 2.2) indicates values of about 4.4, 13 and 14.4 nm for the γ -Fe₂O₃/Fe₃O₄, Fe₃C, and α -Fe phases, respectively. An accurate differentiation between the various crystallographic phases is rendered difficult by the asymmetry of the line graph (mostly due to the overlapping peaks). The Fe peaks in particular, seem to be partially hidden by the dominant carbide phases. More information about the structural aspects of the chemical components of sample F3 can be derived from the Mössbauer analysis (see Fig. 2.3).

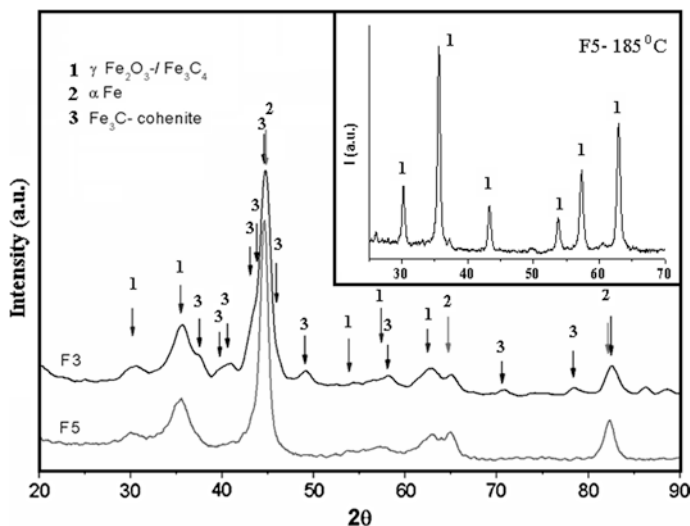


Fig. 2.3 XRD characterization of the as-synthesized samples F3 (*upper curve*) and F5 (*lower curve*). In the inset, the diffractogram of the heated F5 sample at 185 °C is presented

2.3.4 TEM Analysis

To obtain data on the particle composition, an EDX analysis was carried out for all SF and F samples (Table 2.3). A variety of scans over a wide sample area showed a rather constant concentration of Fe, O and C throughout the material. The Fe/O atomic ratio (last column in Table 2.3) for the samples SF32 and SF30 seems close to the value of bulk maghemite iron oxide of 0.67 atomic percent (at%). At the same time, the increased Fe/O ratio for samples F3 and F5 could account for the co-existence of the iron oxide with other Fe compounds (such as iron carbides and/or metallic iron). Most probably, the presence of carbon is mainly due to the synthesis method, in which unwanted decomposition of C₂H₄ could occur. This process increases significantly with increased reaction temperature (i.e., increased laser power). We may therefore observe that the carbon content increases from 9.8 to 13.8 at% for laser powers of 35 and 55 W (sample SF32 vs. SF30) and from 15.6 to 24.5 at% for laser powers of 25 and 65 W (sample F5 vs. F3).

The TEM analysis of samples SF32 and SF30 reveals an almost polycrystalline morphology (Fig. 2.4a, b). The nanoparticles show coalescent features. Cross-linked chains may sometimes be observed. The image of SF30 displays mostly faceted particles. Rather spherical nanoparticles (form factor $k = 0.86$) are revealed for sample SF32. The left insets in Fig. 2.4 present the histograms of particle size distributions. By a lognormal fitting, rather sharp particle diameter

Table 2.3 Comparative EDAX analysis of SF and F samples

	Fe _K (at%)	O _K (at%)	C _K (at%)	Fe/O
SF30	32.1	54.1	13.8	0.59
F3	47.2	28.3	24.5	1.67
SF32	35.1	55.1	9.8	0.64
F5	51.9	32.5	15.6	1.60

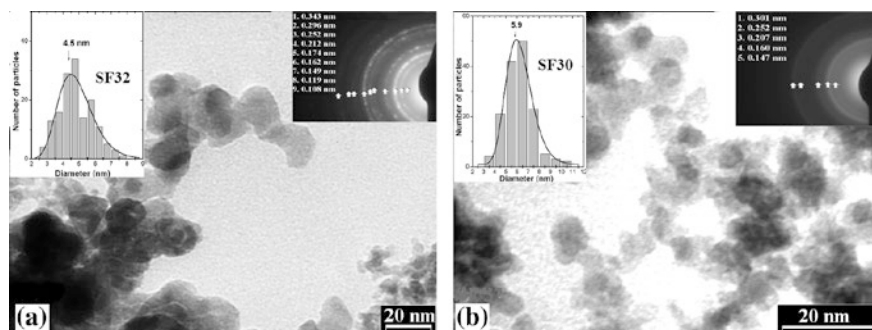


Fig. 2.4 TEM analysis of iron oxides obtained from: **a** sample SF32 and **b** sample SF30. The particle size distributions are presented inside the left insets. SAED patterns of samples SF32 and SF30, revealing main diffraction rings of maghemite/magnetite are presented inside the right insets

distributions are found, with maxima at $dm = 4.5$ and 5.9 nm, for SF32 and SF30. A tendency for increased mean particle diameter with increasing laser power may be observed.

An SAED analysis for both SF samples (presented inside the right insets in Fig. 2.4a, b) shows the cubic structure of the iron oxide, namely maghemite/magnetite. For both samples the strong diffraction rings at 0.25 and at 0.14 nm are noticed. As mentioned before, it is difficult to differentiate between these phases by using only diffraction techniques due to the closed values of their reflections. The electron diffraction pattern of sample SF32 (Fig. 2.4a) shows rather diffuse and blurred rings that possibly point to an incomplete crystallization and/or structural defects inside the nanograins. The nanomaterial obtained at higher laser power seems to be characterized by an increased crystallinity. This can be considered as a consequence of both the higher temperature gradients in the reaction zone and the fast quenching of the condensed nanoparticles in the condensation zone of the laser pyrolysis.

A TEM analysis of samples F3 and F5, obtained by the second oxidation procedure, are presented in Fig. 2.5a, b, respectively. Both samples reveal morphologies consisting of a majority of core-shell particles, with various thicknesses of the shells. The nanoparticles show coalescent features and cross-linked chains.

The right insets in Fig. 2.5 present the histograms of particle size distributions. In the case of the high power synthesis of samples F (Fig. 2.5a), a mean diameter

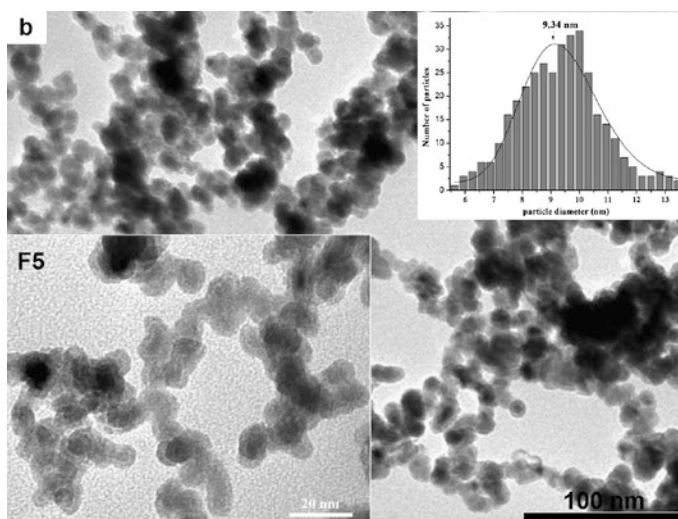


Fig. 2.5 TEM analysis of iron oxides obtained from: **a** sample F3 and **b** sample F5. The particle size distributions are presented inside the right insets

of about 10.6 nm is estimated. There is a decrease of the mean particle diameter with decreased laser power (not presented here). Broader particle distributions are found for samples F compared to those of samples SF (extending to about 10 nm).

2.3.5 Magnetic Properties of the Iron Nano-Oxide Particles Produced by Laser Pyrolysis

Magnetization curves obtained at 300 K for the representative samples of the SF and F series are displayed in Fig. 2.6 in the range from -800 to 800 kA/m. It shows the variation of magnetization M as a function of externally applied magnetic field H (measured in the SI units).

It is worth mentioning that none of the samples are saturated at the maximum available field of 800 kA/m. Excepting the ferrimagnetic type of coupling, this behavior can be considered at a certain extent also an evidence for a disordered spin configuration, connected with the defected structure inside nanoparticles and in agreement with the Mössbauer data (see Fig. 2.6). The magnetization at the maximum field has been denoted as M_S (specific magnetization). The specific magnetization of the SF30 sample, 46 emu/g, is much larger than for the other SF sample (16 emu/g for SF32). Two reasons might contribute to the rather different specific magnetization of the samples: either a different magnetic phase composition or a different “magnetic disorder” connected to a different structural disorder. More defects and lattice disorders in SF32 compared to SF30 seem likely when considering the XRD diffraction patterns as well as the lower average size of the particles in SF32.

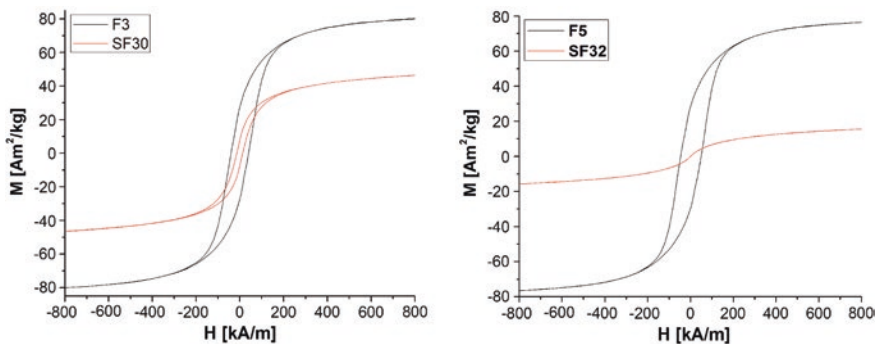


Fig. 2.6 Magnetization of the high-power laser samples SF30 and F3 (*upper curves*) compared to low-power laser samples SF32 and F5 (*lower curves*)

On the other hand, M_s has significantly higher values for F3 and F5 (80 and 78.5 emu/g, respectively) when compared to the SF samples. Here, the effect of the α -Fe phase, whose presence in the F samples was revealed by a XRD analysis, has to be considered (the room temperature magnetization for bulk Fe is about $220 \text{ Am}^2/\text{kg}^{23}$). With regards to the coercivity, it is worth noting that the higher values obtained for F samples (40–48 kA/m) are in agreement with the agglomeration of the larger particles in those samples, giving rise to extended magnetic domains. On the other hand, the SF samples show either a superparamagnetic behavior of mono-domain nano-particles (H_c is about zero for sample SF32), or a mixture of superparamagnetic particles and agglomerated particles giving rise to less pinned magnetic domains ($H_c = 13 \text{ kA/m}$ for sample SF30).

For samples SF32 and SF30, the study of the Mössbauer spectra and of the derived blocking temperatures (of about 200 and 400 K, respectively) was performed [for more details see reference Teunissen et al. (2001)] Accordingly, average particle sizes of about 7 and 9 nm were estimated for samples SF32 and SF30 by considering noninteracting nanoparticles and average magnetic anisotropy constants of bulk magnetite and maghemite (Dumitrache et al. 2005). These average magnetic sizes are almost double compared to the above mentioned physical (TEM) and structural (XRD) ones.

2.4 Core-Shell Iron-Carbon Nanocomposites

2.4.1 State of the Art

In the following, we focus on magnetic iron-core carbon-shell nanoparticles. The major role of the nonmagnetic shell is to protect the functional core from damaging environments like oxygen, as well as to render the nanoscopic colloids water-soluble or even make them compatible with biological media (Hare et al. 1996). A better alternative to the polymer and silica coatings often employed in

literature is represented by coating with carbon-based materials. These coatings have the major advantage of a higher chemical and thermal stability and are in addition biocompatible. Well-developed graphitic carbon layers can be formed around metal nanoparticles by arc-discharge, laser ablation and electron irradiation, using a variety of organic molecules as the carbon source. These carbon layers provide effective barriers against oxidation and acidic corrosion. Moreover, they are easily formed around metal nanoparticles, which are usually more difficult to coat than corresponding oxides but have better magnetic properties. Unfortunately, carbon-coated nanoparticles are often not obtained as well-defined monodisperse cores but as agglomerated clusters since their formation mechanism and synthetic methods are not yet fully understood. Therefore, the preparation of dispersible well-defined carbon-coated core-shell nanoparticles still provides a major challenge in this field. Carbon nano-capsules, filled with metal nanoparticles, have been produced by arc-discharge, ion-beam sputtering methods, via solid-state reaction and chemical methods.

Recently, we have reported the successful fabrication of carbon-encapsulated iron nanoparticles by laser pyrolysis from gas phase precursors (Scheart 2010). The focused continuous wave CO_2 laser radiation (output power maximum 85 W, $k = 10.6 \text{ } \mu\text{m}$) was orthogonally crossed with the reactant gas stream that was admitted to the center of the reaction cell through a triple nozzle system (Fig. 2.7).

The four representative Fe@C samples (labeled CF40–CF43) are presented in Table 2.4. They were obtained at different internal diameters of the central nozzle (varying from 0.55 to 1.5 mm). C_2H_4 was used as sensitizer. It absorbs the energy from the CO_2 laser radiation and transfers it by collision to the other reaction partners. The laser power, the pressure in the reaction cell, the flows of acetylene and ethylene were maintained at 85 W, 650 mbar, 100 and 30 sccm, respectively. The flame temperature was monitored with an optic pyrometer.

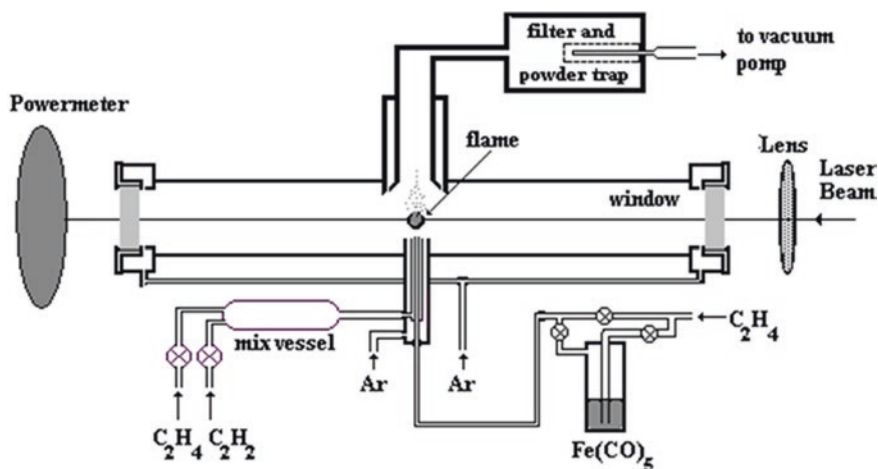


Fig. 2.7 Schematic of the laser pyrolysis installation for the synthesis of Fe@C nanocomposites

Table 2.4 Experimental parameters for the laser synthesized CF samples^a. The element analysis (EDAX) and the mean crystallite sizes as evaluated from XRD analysis

Sample	C ₂ H ₄ through Fe(CO) ₅ sccm	C ₂ H ₄ (middle) sccm	Internal nozzle diameter mm	τ Estimated residence time (10^{-3} s)	EDAX At%			XRD—Mean crystallite sizes (nm)	
					Clk	Ok	Fek	α -Fe	FexCy
CF40	50	30	0.55	0.22	76.80	13.30	9.9	10.5	1.4
CF41	50	30	0.9	0.59	81.36	8.77	9.73	10.0	1.5
CF42	50	30	1.3	1.21	78.10	7.30	14.60	22.3	2.3
CF43	50	30	1.5	1.50	72.86	8.18	18.96	25.0	8.4 (Fe3C phase)

^aThe total pressure (650 mbar), the laser power (85 W), the acetylene flow (100 sccm) and the Argon flows (for confinement and windows clearing) were maintained constant (1,100 and 150 sccm, respectively)

The element compositions (Fe, C and O) were evaluated via X-ray energy dispersive analysis (EDAX) and are presented in Table 2.4. One may observe the large carbon quantity (around 70–80 at%) which probably enters in the carbon matrix surrounding iron-based nanoparticles (partly as iron carbides). In this respect, it is worth noting that the EDAX reveals the highest iron content in the sample with the larger nozzle (sample CF43).

In order to describe the growth of Fe@C nanoparticles in the laser pyrolysis, we refer to a model for the formation of SiC, proposed in 1994 by Lihrmann and Cauchetier which is based on the decomposition of the reactants in the laser pyrolysis flame, followed by growth from collisions and coalescence (Lihrmann and Cauchetier 1994). Thus we consider that intermediate species such as Fe and C are assumed to play a key role in the growth process. The size of the final nano-products is evaluated from the residence time within the flame. The residence time inside the flame is considered equivalent to the time of residence in the laser beam (t) and can be estimated from the total gas flow velocity (v), $t = d/v$, where d is the diameter of the laser beam (0.4 cm). The velocity v is considered proportional to the gas flow rate (in cm^3/min) and to the temperature T (K) and inverse proportional to the nozzle surface (cm^2) and to the working pressure P (mbar) (Dumitrache et al. 2003). Even if C_2H_4 plays the role of a sensitizer in the precursor mixer, its partial decomposition cannot be overruled and could contribute to the graphenic sheets of the particle coverage.

2.4.2 XRD Analysis

A comprehensive XRD analysis of the four generic Fe@C samples first analyzes the common features of samples CF40, CF41 and CF42. The diffractogram for sample CF40 is presented in Fig. 2.9 and reveals a large peak in the 2θ 40–46 domain, in which the higher intensity peak of α -Fe ($2\theta = 44.712$) overlaps the characteristic region of iron carbide. The broad maximum characterizes a quasi-amorphous iron/iron carbide phase [FeC , Fe_2C , Fe_7C_3 or Fe_3C (with lower carbon content)], possibly indicating that transformation and constitution/crystallization processes occur in the region of the iron carbide maxima. Also visible are the other two peaks of α -Fe (at $2\theta = 65.082$ and 82.146). In Fig. 2.9, where the two XRD patterns of samples CF40 and CF43 are superposed, the large peak in the region of the iron carbide maxima phases (they are labeled Fe_xC_y in Table 2.4) is also presented. The diffraction pattern of sample CF43 exhibits a higher crystallinity than that of sample CF40 (Fig. 2.8).

The estimation of mean crystallite dimensions (the values are listed in Table 2.4) was performed using the Scherrer formula. The Voigt function was used for the approximation of the profile maximum at $2\theta = 44.712$. When looking at the estimated values of the Fe crystallite dimensions of sample CF43, one finds that they are higher than for sample CF40. Larger mean crystallite sizes are revealed, whose dimensions slightly increase with the increased nozzle diameter (from about 10 nm to about 25 nm, for sample CF40 to CF43). It is however

Fig. 2.8 The XRD analysis of sample CF43. Marked with red are the characteristic diffraction peaks of Fe_3C cementite

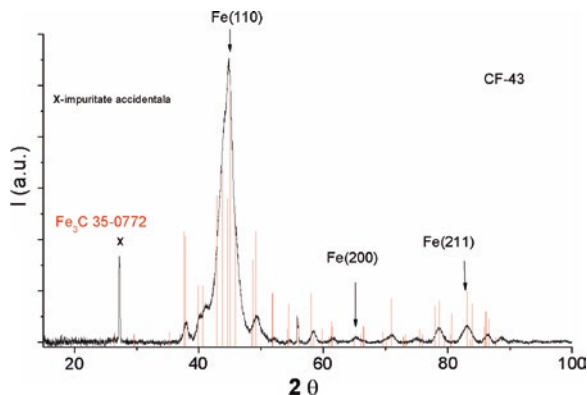
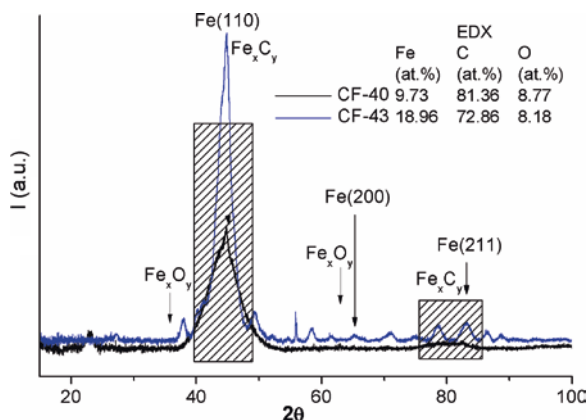


Fig. 2.9 Comparison between the diffraction patterns of samples CF40 and CF43. Dashed contours separate the characteristic diffraction regions of Fe_3C . The inset presents the elemental values given by EDX analysis for the two samples



possible that only a minor part of the Fe phase is represented by large Fe crystallites while a more amorphous Fe phase could be represented by much smaller crystallites, which are not detected by the XRD analysis. We could characterize the material as constituted by very low dimension crystalline domains, which do not extend enough to form a defined crystalline phase. In case of sample CF43, the carbide phase clearly indicates the formation of the crystalline Fe_3C -cementite phase, with higher Fe_3C mean crystallite dimensions (about 8.4 nm diameter).

2.4.3 TEM Analysis

TEM analysis of the nanocomposite morphology reveals mostly particles that seem encapsulated in an amorphous matrix. TEM images of samples CF40 and CF43 are presented in Fig. 2.10a, b, respectively.

The histograms (lognormal fit) of particle size distributions are presented in Fig. 2.11. Rather sharp particle diameter distributions are found, with maxima

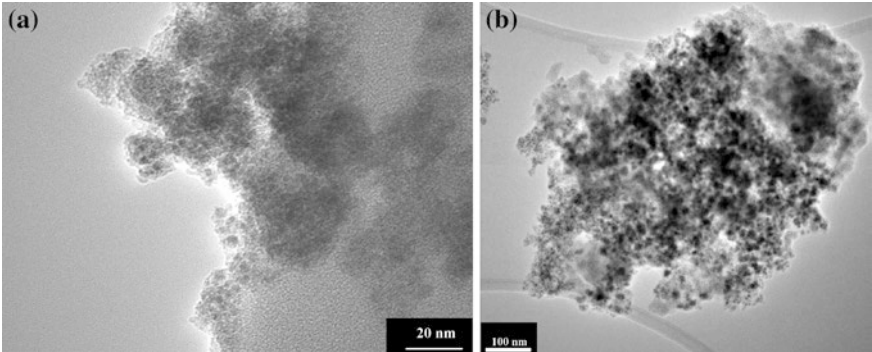


Fig. 2.10 TEM images of samples CF40 (a) and CF43 (b)

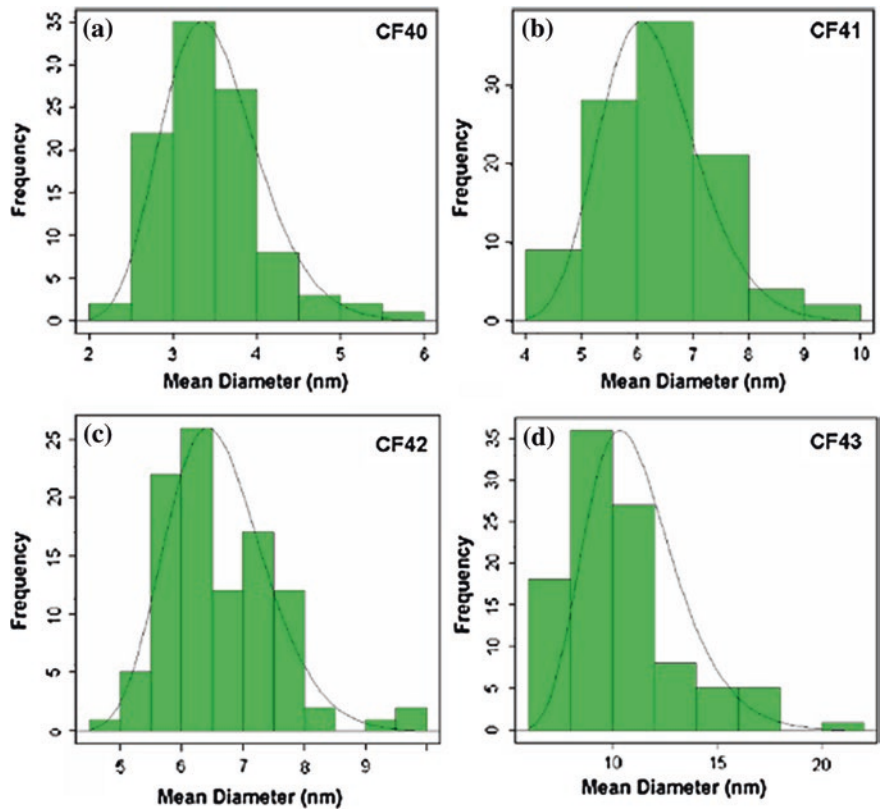


Fig. 2.11 a, b, c and d. Particle size distributions for the representative samples, evidencing increased mean particle diameter (from around 3.5 nm to around 10.5 nm) with increasing diameter of the inner nozzle

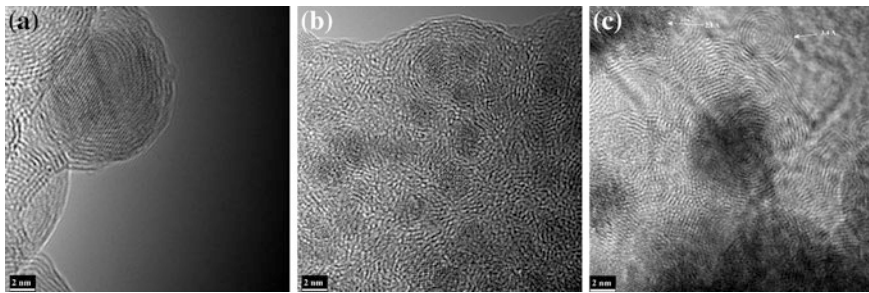


Fig. 2.12 HRTEM images of the sample CF43: well distinguishable round iron core of about 11 nm diameter (showing an identified interplanar distance of $d = 2.1 \text{ \AA}$ for Fe/Fe₃C) surrounded by graphene layers (a); agglomerated iron-based nanoparticles (dark contrasts) separated by a varying number of graphene sheets

at about $d_m = 3.5, 5.7, 6.4$ and 10.5 nm, for CF40, CF41, CF42 and CF43, respectively. An increasing mean particle diameter with increasing internal nozzle diameter may be noticed.

HRTEM images of the CF43 nanoparticles are presented in Fig. 2.12. The sample reveals a morphology consisting of a majority of core-shell particles, with various thicknesses of the shells. Agglomerated iron-based nanoparticles (dark contrast) separated by a varying number of graphene sheets and onion-like shape of the surrounding carbonaceous layers often appear. In Fig. 2.12a, the well distinguishable round iron core (of about 11 nm diameter) shows an identified interplanar distance of $d = 2.1 \text{ \AA}$ (which belongs to Fe/Fe₃C cementite). This core is surrounded by about eight graphene layers with identified interplanar distance of $d = 3.5 \text{ \AA}$, which is close to that of the graphitic carbon.

2.4.4 Magnetic Analysis

The magnetization curves obtained at 300 K for the representative Fe@C samples are displayed in Fig. 2.13a in the range from -800 to $+800$ kA/m and in Fig. 2.13b in the range from -25 to $+25$ kA/m (detail around the origin). They show the variation of the magnetization M as a function of the external applied magnetic field H . One may observe that for the samples CF40 and CF41 the hysteresis loops are missing. The superparamagnetism of these samples is largely due to their mean particle dimensions (equal or much less than 10 nm, for the Fe and the iron carbide phases, respectively, as determined by XRD). The magnetization at the maximum field has been denoted as M_S (saturation magnetization). The saturation magnetization of 65.9 emu/g of the sample CF43 is much greater than that for the other CF samples, particularly of sample CF40 (28.38 emu/g). More defects and lattice disorder in CF40 in comparison to CF43 can be assumed. It is worth mentioning that none of the samples are saturated at the maximum available field of 800 kA/m.

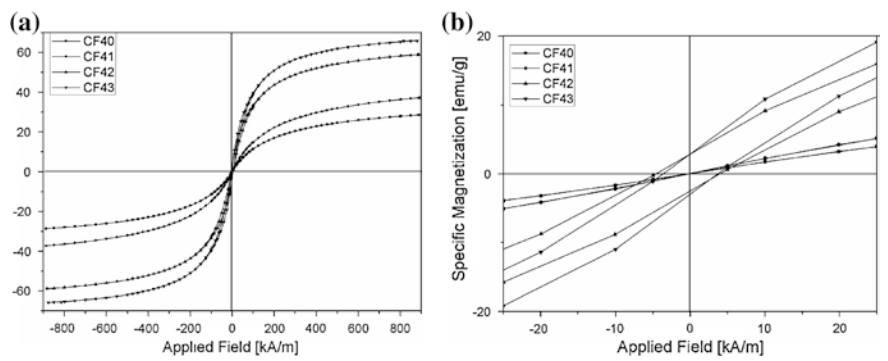
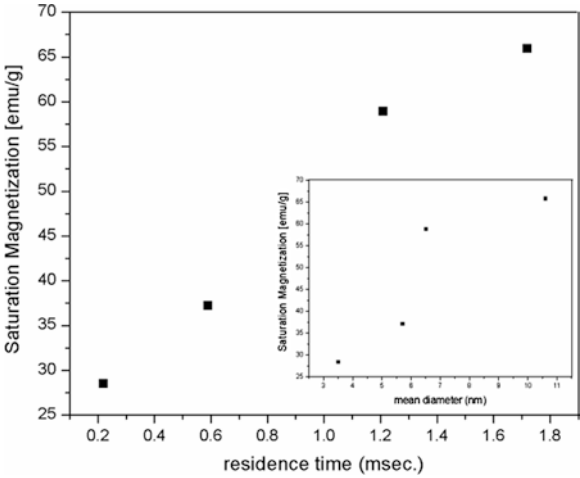


Fig. 2.13 Magnetization curves of the Fe@C samples obtained by laser pyrolysis with different diameters of the internal nozzle (a). Detail from Fig. 2.13 for the domain $-25 \text{ kA/m} \leq H \leq 25 \text{ kA/m}$ (around origin) (b)

Fig. 2.14 The variation of the saturation magnetization (in $\text{A m}^2/\text{kg}$) of Fe@C nanoparticles with the residence time. The inset displays the increasing trend of the saturation magnetization with increasing Fe@C mean particle size



This behavior can be considered at a certain extent also an evidence for a disordered spin configuration. As to the magnetic disorder, more defects and lattice disorder in CF40 compared to CF43 are easily explained by the XRD diffraction patterns. One may observe a direct correlation between the residence time in the laser beam and the saturation magnetization (see Fig. 2.14). For all four representative samples discussed here, the magnetization M at the maximum H values increases as the residence time increases, i.e., the dominance of a mixture of crystalline cementite-iron carbide and of the α -Fe phase becomes apparent. Here we can refer to the literature (Madler et al. 2002) where a saturation magnetization value of 110 emu/g was found. On the other hand, the effect of the α -Fe phase (with a higher contribution in sample CF43, as revealed by XRD analysis) has to be considered (the room temperature magnetism).

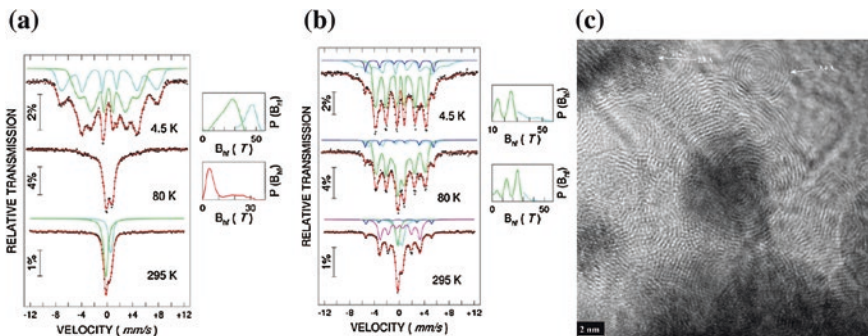


Fig. 2.15 Mössbauer spectra at different representative temperatures for sample CF40 (a); Mössbauer spectra at different representative temperatures for sample CF43 (b)

The Fe phase composition was studied by a temperature dependent ^{57}Fe Mössbauer spectroscopy. Figure 2.15a, b present the Mössbauer spectra for samples CF40 and CF43, respectively. The derived probability distributions of the hyperfine field are presented at the right side of the figures. By means of a Mössbauer spectroscopy one can perform a phase analysis of the magnetic component as well as an analysis of the magnetic relaxation. This is especially valid at low temperatures where spin dynamic effects may be eliminated. In case of nanoparticles with distributions of particle dimensions, it is possible to have different phase compositions for particles of different sizes. The phase information obtained at low temperatures should be correlated with the development of the magnetic relaxation.

Sample CF43 (Fig. 2.15b), obtained at the largest diameter of the inner nozzle, presents three distinct phases, i.e., the two phases mentioned before (for CF40) and another phase which is characterized in the Mössbauer spectrum by a sextet with a hyperfine field of 34 T, specific to the bcc iron. The 4.5 K spectrum evidences 27 % oxide phase, 6 % bcc iron and 67 % iron carbide. The probability distribution corresponding to the carbide phase presents two peaks (at 15 T and at 24 T), which suggest the superposition of two phases (a major cementite Fe_3C phase and another carbide phase Fe_5C_2). At room temperature, the oxide phase appears in a magnetically relaxed state. As to the carbide phase, only about 15 % is in a relaxed phase while 50 % of it, together with the 7 % iron phase, remains ferromagnetic. This behavior could indicate the presence of two particle types, namely oxide particles with a blocking temperature below 80 K and particles of carbides and carbides with metallic cores, with a blocking temperature above 100 K.

If we analyze the ratio of iron carbide to bcc iron at different temperatures we may deduce that the magnetic relaxation mainly affects the carbide phase while the iron-containing carbide phase relaxes at much higher temperature. Summarizing, at 295 K, the oxide particles, as well as a fraction of 15 % of the carbides, are superparamagnetic. The rest of the particles (6 % metallic Fe and 50 % iron carbide—most of them with core-shell structures) are ferromagnetic at room temperature.

2.5 Conclusion

Iron-based nanomaterials have found applications in many areas of science and technology due to their unique magnetic properties. A size reduction of these materials from bulk to the nanoscale allows them to display various size related properties. Among other changes, a significant decrease in size can alter reactivity, increase surface area and change the magnetic properties.

The synthesis of iron oxide-based nanomaterials by laser pyrolysis has been achieved by a handling procedure (standard), in which the oxidation process initiates and develops inside the laser-induced reaction zone (samples SF). In a second step, a more complex experimental procedure is used, in which the iron precursor is allowed to dissociate alone in the flame with a surrounding oxidizing atmosphere (samples F).

XRD and TEM analyses reveal a major content of maghemite/magnetite in samples SF. A mixture of three iron-based phases, namely γ -Fe₂O₃/Fe₃O₄ iron oxide, cementite Fe₃C and metallic Fe phase is found in samples F. The relative proportion of these phases depends on the reaction temperature (laser power). Agglomerated core-shell structures are often observed. For both kinds of samples, the crystallinity (crystallographic order) is enhanced by increasing the laser power. As determined by TEM, mean particle sizes depend on the laser power density and vary between about 4 and 6 nm for samples SF and between about 9 and 11 nm for samples F. By controlled heating of samples F (maximum temperature 185 °C), a pure crystalline maghemite/magnetite oxide phase was found as well as an increase of mean particle diameters.

Looking at the hysteresis loops at room temperature, one finds that the saturation magnetization values of samples F are much higher (about 80 Am²/kg) compared to the samples SF (between 16 and 46 Am²/kg). Depending on the laser power, either superparamagnetic or a superposition of superparamagnetic and ferromagnetic behavior are exhibited by the samples SF at room temperature. Agglomerations of the larger particles give rise to a magnetic domain structure and to enhanced coercive forces in samples F.

The temperature dependent Mössbauer measurements confirm the formation of larger particles at higher laser power densities as well as the presence of inter-particle magnetic interactions. For samples SF, more than 90 % of the particles are formed by defected maghemite/magnetite mixtures and only 5–10 % are of cementite. The much lower specific magnetization, as compared with the expected one from the Mössbauer phase composition, is due to a large quantity of defected structures of the nanoparticles.

Well crystallized Fe phases are observed in the F samples. Regarding the oxide phase in sample F5, the particles are either fully oxidized or they form a core (α -Fe)-shell (Fe oxide) structure. Relatively thicker oxide shells are found for higher laser power densities, when larger particles are formed. The rest of the particles (about 15 %) are made up by defected cementite. For sample F3 a more complex composition is deduced comprising of an α -Fe phase (17 %) surrounded

by Fe-oxide shells (10 %) fully oxidized superparamagnetic particles (30 %) and a well crystallized cementite phase (14 %) surrounded by defected cementite (30 %).

In a third step, we have demonstrated the synthesis of iron-core oxide-shell nanocomposite by a two-step method: the laser pyrolysis of an iron pentacarbonyl and ethylene mixture followed by a controlled step-by-step passivation process. Iron particles with 14 nm mean diameter and about 4 nm oxide shell thickness were produced. The morphology of the nanocomposite particles was determined. They are made up by an α -Fe core surrounded by an γ -Fe₂O₃/Fe₃O₄ shell.

Based on the versatility of the laser technique (exemplified here by different oxidizing processes based on gas-handling procedures) further variations of the experimental conditions are pursued in order to prepare optimized magnetic iron-based nanostructures.

Iron-based carbon core-shell Fe@C nanostructures were produced by the one-step laser pyrolysis technique. An acetylene/ethylene mixture was used as carbon precursor. The possibility to vary the chemical content and the nanoparticle dimensions by varying the nozzle diameter of the emergent reactive gas flow (from 0.55 to 1.5 mm diameter) is demonstrated. The XRD analysis shows that at increased nozzle diameter, an increased ordering of the crystallographic network is apparent, with dominant α -Fe and Fe₃C iron carbide phases. EDAX reveals the highest Fe content for the sample produced with the larger nozzle diameter. TEM images of the Fe@C particles and the histograms of the particle size distributions suggest the increase of the particle diameter (from about 3.5 to 10.5 nm) with increasing nozzle diameter. Onion-like surrounding graphenic layers often cover the buried iron-based (Fe/Fe₃C) cores. The magnetic measurements of the composite nanoparticles indicate an almost direct correlation between the residence time in the laser beam and the saturation magnetization. Complementary details of the Fe phase composition and the superparamagnetic character of the samples are provided by the Mössbauer analysis. Experiments for obtaining stable water-based magnetic nanofluids from Fe@C nanoparticle precursors are under way.

References

- Abhilash, K Revati, Pandey BD (2011) Microbial synthesis of iron-based nanomaterials for biomedical applications—review. *Bull. Mater. Sci.*, 34(2):191–198 (*J. Phys.: Conf. Ser.* 332 012042)
- Baena J, Marulanda JI (2011) Analysis of chemical processes for the synthesis of magnetite for biomedical applications. *J Phys: Conf Ser* 332:012042
- Blanco-Andujar C, Tunge LD, Thanh NTK (2010) Synthesis of nanoparticles for biomedical applications. *Annu Rep Prog Chem, Sect A* 106:553–568
- Bolden NW, Rangari VK, Jeelani S, Boyoglu S, Singh SR (2013) Synthesis and evaluation of magnetic nanoparticles for biomedical applications. *J Nanopart* 2013, Article ID 370812 (9 pages)
- Bomatí-Miguel O, Zhao XQ, Martelli S, Di Nunzio PE, Veintemillas-Verdaguer S (2010) Modeling of the laser pyrolysis process by means of the aerosol theory: case of iron nanoparticles. *J Appl Phys* 107:014906(7 pages)
- Cannon WR, Danforth SC, Flint JH, Haggerty JS, Marra RA (1982) Sinterable ceramic powders from laser driven reactions, Part 1: Process description and modeling. *J Am Ceram Soc* 65:324

- Dumitrache F, Morjan I, Alexandrescu R, Ciupina V, Prodan G, Voicu I, Fleaca C, Albu L, Savoiu M, Sandu I, Popovici E, Soare I (2005) Iron-Iron oxide core-shell nanoparticles synthesized by laser pyrolysis followed by superficial oxidation. *Appl Surf Sci* 247:25–31
- Dumitrache F, Morjan I, Alexandrescu R, Morjan RE, Voicu I, Sandu I, Soare I, Ploscaru M, Fleaca C, Ciupina V, Prodan G, Rand B, Brydson R, Woodward A (2003) Nearly monodispersed carbon coated iron nanoparticles for the catalytic growth of nanotubes/nanofibres. *Diam Relat Mater* 13(2):362–370
- Einar Kruis F, Fissan Heinz, Peled Aaron (1998) Synthesis of nanoparticles in the gas phase for electronic, optical and magnetic applications—a review. *J Aerosol Sci* 29(5–6):511–535
- Hare JP, Hsu WK, Kroto HW, Lapas A, Prassides K, Terrones M, Walton DRM (1996) Nanoscale encapsulation of molybdenum carbide in carbon clusters. *Chem Matter Commun* 8:6–8
- Kuncser V, Schinteie G, Sahoo B, Keune W, Bica D, Vékás L, Filoti G (2007) *J Phys: Condens Matter* 19:016205
- Lihrmann SJM, Cauchetier M (1994) A model for the formation of nanosized SiC powders by laser induced gas phase reaction. *J Eur Ceram Soc* 13:41. (Studies of Fe(CO)₅)
- Madler L, Kammler HK, Mueller R, Pratsinis SE (2002) Controlled synthesis of nanostructured particles by flame spray pyrolysis. *J Aerosol Sci* 33(2):369–389(21)
- Majima T, Matsumoto Y, Takami M (1993) On the SF₆-sensitized IR photodecomposition of Fe(CO)₅: 5 μm transient absorption measurements and absorption energy measurements. *J Photochem Photobiol, A* 71:213
- Scheart Wolfgang (2010) Current directions in core-shell nanoparticle design. *Nanoscale* 2:829–843
- Shikwambana L, Govender M, Mwakikunga B, Sideras-Haddad E, Forbes A (2011) A review of the laser pyrolysis technique used to synthesize vanadium and tungsten oxide thin films. *Adv Mater Res* 227:80–83
- Srdic VV, Winterer M, Hahn H (2000) Sintering behavior of nanocrystalline zirconia prepared by chemical Vapor synthesis. *J Am Ceramic Soc* 83:729
- Swihart MT (2003) Vapor-phase synthesis of nanoparticles. *Curr Opin Colloid Interface Sci* 8:127
- Teunissen W, de Groot FMF, Geus J, Stephan O, Tence M, Colliex C (2001) The structure of carbon encapsulated NiFe nanoparticles. *J Catal* 204:169–174
- Veintemillas-Verdaguer S, Morales MP, Serna CJ (2001) *Appl Organomet Chem* 15:365

Upscaling of Bio-Nano-Processes

Selective Bioseparation by Magnetic Particles

Nirschl, H.; Keller, K. (Eds.)

2014, XVII, 245 p. 141 illus., 29 illus. in color.,

Hardcover

ISBN: 978-3-662-43898-5